RSC Advances

PAPER

View Article Online
View Journal | View Issue

Cite this: *RSC Adv.*, 2025, **15**, 24087

Uncovering three-body competition of chain growth, degradation and re-aggregation for polyphenylacetylenes during solution polymerization†

Wenjie He, Lin Zhou, Jinxian Yang,* Mo Zhu * and Lianwei Li*

By employing phenylacetylene as a model system to understand the structural evolution of conjugated polymers during solution polymerization, we reveal for the first time the three-body competition mechanism involving chain growth, degradation, and re-aggregation processes in poly(phenylacetylene) (PPA) synthesis. Key findings include: (1) identification of a universal two-stage degradation phenomenon (5.0 min < time < 200 h) independent of solvent or atmosphere, comprising a slow polymerization-dominated degradation of large fragments followed by rapid degradation-dominated breakdown of smaller fragments; (2) demonstrated solvent- and atmosphere-dependent relationships for maximum conversion, apparent molar mass ($M_{\mathrm{w,app}}$), and characteristic transition time (t_{transit}), where inert atmosphere and polar solvents prolong t_{transit}, indicating distinct activation energies for thermal-*versus* oxidative degradation pathways; (3) quantification through light scattering of absolute-to-apparent molar mass ratios ($M_{\mathrm{w,abs}}/M_{\mathrm{w,app}} = 2.3\text{–}3.3$) across solvents, establishing a critical conversion factor for molecular weight comparisons in conjugated polymer studies. Simplified component analysis combining $M_{\mathrm{w,abs}}$, average hydrodynamic radius ($\langle R_{\mathrm{h}}\rangle$), and size distribution ($f(R_{\mathrm{h}})$) further unveils an unexpected competition between degradation (1–10 nm fragments) and re-aggregation (40–400 nm clusters) in dilute solutions. Our results suggest SEC flow fields may disrupt weakly-bound aggregates. This work provides fundamental insights into dynamic competition mechanisms governing conjugated polymer synthesis, with implications for controlled fabrication of polymeric architectures.

Received 1st May 2025
Accepted 18th June 2025

DOI: 10.1039/d5ra03067f

rsc.li/rsc-advances

1 Introduction

Conjugated polymers feature a unique structure where π electrons are shared between structural units, forming a continuous conjugated semiconductive structure. This arrangement facilitates energy level splitting and enables electron excitation, imparting outstanding optical, charge-transport, and conductive properties to the polymers.[1] Conjugated polymers, which combine the conductive properties of metals (through doping) and semiconductors with the processability of polymers, have been extensively applied in various energy and materials fields.[2,3] Representative architectures such as conjugated ladder polymers, double-bond-linked conjugated polymers, and conformation-locked conjugated polymers[4] are widely used in conductive hydrogels,[5,6] flexible electronic sensors,[7–9] and photocatalytic reactions.[10,11] Porous conjugated polymers, especially covalent organic frameworks (COFs), are gaining prominence as efficient heterogeneous photocatalysts.[12,13]

The optoelectronic performance of conjugated polymers is intricately tied to their chain structure, degradation, and aggregation behavior. A systematic understanding of the interplay between stability and degradation across synthesis, purification, film formation, and application stages is crucial for maintaining their performance integrity. Current studies have demonstrated that environmental factors such as oxygen, solvents, light, and heat[14–18] exert substantial influence on the stability and degradation of conjugated polymers in both bulk and solution states. These factors and their synergistic effects have attracted considerable research interest in both academia and industry. In the solution state, degradation processes are driven by multiple mechanisms, including photo-induced conformational shifts,[19] cross-linking,[20] oxidation by oxygen causing main chain bond cleavage,[21,22] and thermal chain isomerization and degradation.[23–25] In the bulk state or film form, polymer chain degradation compromises mechanical integrity and optoelectronic properties, manifested in alterations to absorption spectra, energy levels, charge carrier mobility, and interface characteristics, ultimately diminishing

---

College of Chemistry and Environmental Engineering, Shenzhen University, Shenzhen 518060, China. E-mail: lianweili@szu.edu.cn

† Electronic supplementary information (ESI) available. See DOI: https://doi.org/10.1039/d5ra03067f

photovoltaic efficiency and operational lifespan. Significantly, research has shown that during synthesis/purification techniques such as solution polymerization, precipitation separation, spin-coating (film processing), the molecular conformation and aggregation of conjugated polymers generally retain structural integrity.[26–29] However, many studies employ discrete experimental approaches, overlooking concurrent polymerization and degradation reactions, resulting in incomplete understanding of their competitive mechanisms.

Taking polyphenylacetylene (PPA) and its derivatives as representative model systems of conjugated polymers, most previous studies have concentrated on isolated investigations of the polymerization mechanism, structure–property relationship, and degradation process. However, no systematic research has been conducted on the competition between chain-growth and degradation during the solution-phase polymerization of phenylacetylene (PA). Specifically, in polymerization mechanism studies, Morokuma *et al.* utilized a diene-Rh catalyst system and computational approaches to elucidate the polymerization mechanism of PPA. They discovered that PA predominantly undergoes 2,1-insertion, with kinetic disparities originating from chain-propagating conformational restrictions in the transition state. This provides a theoretical foundation and design principles for developing efficient PPA catalysts with tailored structures[30] Nishimura *et al.* introduced a versatile method for controlled living polymerization of phenylacetylene *via* a multicomponent catalytic system, establishing a platform for terminal functionalization of PPA.[31–33]

Félix Freire *et al.* utilized PPAs to investigate dynamic helical polymer structures, adjusting helical orientation using external stimuli to generate macroscopic chiral nanostructures.[34–36] Afang Zhang *et al.* examined structure–property relationships in various polymers, including thermosensitive and helical dendritic polymers, using PPA derivatives as models.[37,38] Toshio Masuda *et al.* demonstrated the living polymerization of PA with an Rh-vinyl complex and noted PPAs limited stability in ambient conditions. Further analyses indicated enhanced stability in poly(disubstituted acetylene) derivatives over mono-substituted variants, with stability increasing with the number and size of substituents.[39,40] Jan Sedláček *et al.* employed a size exclusion chromatography (SEC) tracking method to investigate the molecular weight and conformational stability of post-polymerized PPA samples in solution.[41,42] C. Cametti *et al.* synthesized PPA using Rh as catalyst and investigated its molar mass in various organic solvents, including tetrahydrofuran (THF), toluene (Tol), and $CHCl_3$, *via* Laser Light Scattering (LLS). They found that the molar mass increased over time under THF, remained constant in Tol, and decreased in $CHCl_3$. These results indicate that the highly stereoregular PPA obtained with the Rh catalyst undergoes different structural modifications in solution.[43,44] However, these studies often treat the chain polymerization and chain transformation of PPAs in isolation and investigate them separately.

From the foregoing information, it is evident that despite some progress in the field of PPA chain growth and degradation, a deep understanding of the competition between growth and degradation during the process, as well as its kinetic characteristics, is still lacking. Specifically, several issues require further clarification: (1) the kinetic correlation between monomer conversion and polymer molecular structure characteristics (such as molar mass, molar mass distribution, growth/degradation rate ratio) during the polymerization process remains unclear, and real-time tracking and analysis of these processes are insufficient; (2) post-polymerization processing typically employs precipitation separation, which may potentially affect the molecular degradation, molecular structure, and aggregation state, yet these potential impacts have not been sufficiently studied; (3) most research utilizes polymers that have been purified, simplifies the polymer system, potentially failing to reflect the accurate molar mass and structure at the end of polymerization, thus impacting the precise evaluation of polymer properties. *In situ* monitoring and analysis of the polymerization process are still necessary; (4) the molar mass during the polymerization process is routinely determined by SEC, which can only provide the apparent relative molar mass of PPA, lacking the true molar mass information during growth and degradation processes.

In this study, by conducting *in situ* sampling and quantitative analysis of the PPA system, we aim to systematically investigate the competitive kinetics of chain growth, degradation, and reaggregation of PPA. The study is primarily divided into two parts: the competitive dynamics of chain growth and degradation during the polymerization process, and the competitive dynamics of degradation and reaggregation in dilute solutions. Specifically, we employed a rhodium catalyst system and the classic solution polymerization technique as a model PPA polymerization system. By combining SEC, Ultraviolet-Visible Spectroscopy (UV-vis), and LLS technologies, we implemented *in situ* sampling, quantitative dilution, and measurement to evaluate the effects of reaction atmosphere (N_2 and air) and solvent type (Tol, THF, and $CHCl_3$) on the competitive reactions of polymerization and degradation, as well as the degradation–aggregation competition process, including changes in molecular weight, molecular size, and re-aggregation state.

2 Result and discussion

2.1 Possible degradation pathways and experimental design for PPA polymerization

Scheme 1 illustrates the Rh-catalyzed polymerization of PA monomer. Two key degradation pathways are proposed: thermal (pathway 1) and oxidative (pathway 2). In pathway 1, a conformational change from the stable *cis–transoidal* to *cis–cisoidal* structure (the key precursor step) triggers a concerted 6π electrocyclization, resulting in cyclization and chain scission. This mechanism, linked to *transoid–cisoid* isomerization in triene sequences, is well-established and supported by literature.[30,45] In pathway 2, unstable peroxide formation causes chain cleavage. Degradation can occur throughout polymerization for both prepolymers and polymers.[39,45,46] Both extrinsic factors (thermal energy, oxygen) and intrinsic chain characteristics (length, substituents, concentration) govern the competition between chain growth and degradation. This study focuses on identifying key governing factors, particularly reaction solvent and atmospheric conditions.

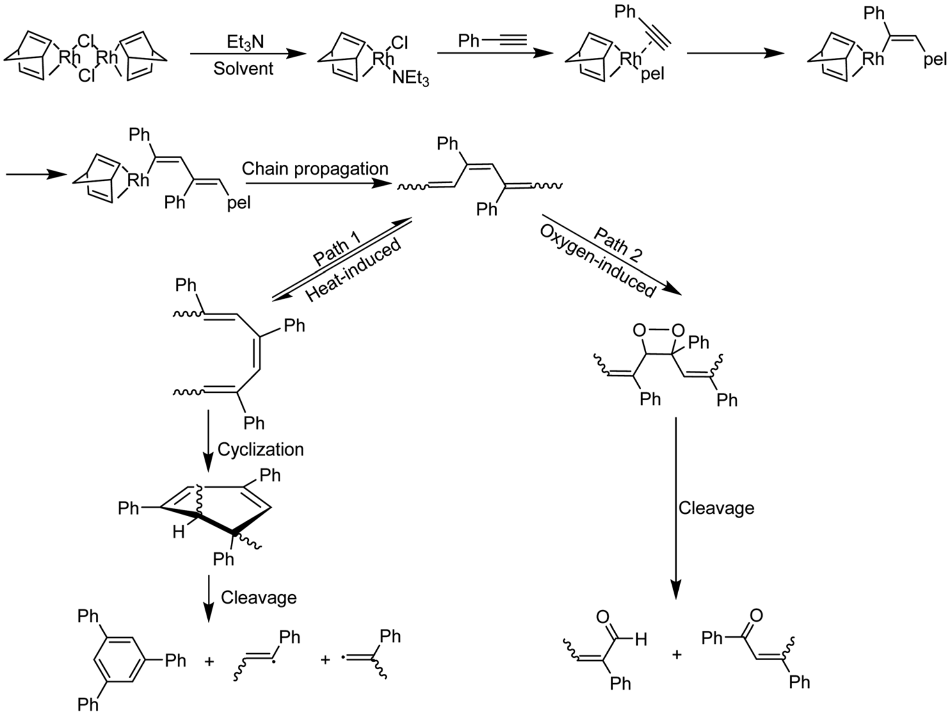

Scheme 1 Schematic illustration of the processes involved in the Rh-catalyzed solution polymerization of PA.

Table 1 summarizes the experimental design for the PPA polymerization in this study, where entries 1–3 and 4–6 were conducted under N_2 and air atmospheres, respectively. Three different solvents were employed: Tol, $CHCl_3$, and THF. To maintain consistency across other variables, taking into account reaction rate, conversion rate, and based on previous literature,[47,48] the feed ratio of [PA]/[Rh]/[Et_3N] was kept constant at 1000/1.0/1.0, with monomer concentration maintained at 50 g L^{-1}. All reactions were performed under constant stirring, thus eliminating variations in PPA degradation caused by differential shear rates (see Fig. S1†). Through this experimental design, we systematically investigated the effects of atmosphere, solvent polarity, and solubility parameters.

2.2 Experimental confirmation of the short-term stability of PPA chains in solution

Prior to gaining insight into the competition between chain growth and degradation during polymerization, it is imperative to establish the short-term stability of PPA polymers in solution, which serves as a fundamental prerequisite for precise physical property measurements and extraction of molecular structure information. However, this critical issue has persisted as a knowledge gap in previous studies. For example, for the LLS measurement to extract the absolute molecular information regarding the mass and size of chains, rapid degradation kinetics of PPA chains in solution would preclude accurate determination of these properties, as these parameters exhibit molar mass dependency.[49–51]

Table 1 Experimental design for the PPA polymerization conditions

			Feed ratio			
No.	Atmosphere	Solvent	PA	[Rh(nbd)Cl]	Et_3N	C (g L^{-1})
1	N_2	Tol	1000	1.0	1.0	50
2	N_2	THF	1000	1.0	1.0	50
3	N_2	$CHCl_3$	1000	1.0	1.0	50
4	Air	Tol	1000	1.0	1.0	50
5	Air	THF	1000	1.0	1.0	50
6	Air	$CHCl_3$	1000	1.0	1.0	50

To investigate the short-term stability of PPA chains in solution, well-purified PPA samples in solid form are preferred. The synthetic protocol for PPA powder production is summarized in detail in the ESI.† Purified PPA powders were redissolved in their respective solvents (Tol, THF, $CHCl_3$), followed by individual centrifugation (7000 rpm, 10 min) to remove insoluble residues prior to SEC analysis of the supernatant.

As illustrated in Fig. 1, SEC results demonstrate negligible curve shifts between $t = 0$ and 1.0 h across all solvent systems (Tol, $CHCl_3$, THF), indicating stable chain integrity within the measurement timeframe. For instance, for Tol solution under N_2 condition, the value of $M_{w,app}$ is 270 and 265 kDa for $t = 0$ and 1.0 h. For $CHCl_3$ under air condition, the value of $M_{w,app}$ is 279 kDa and 274 kDa for $t = 0$ and 1.0 h respectively, showing a slight degradation and a relatively high stability. Specifically, the change in $M_{w,app}$ is confirmed to be ∼1.8%, 2.1%, 1.6%, 2.2%, 1.3%, and 1.8% for Tol-N_2, Tol-air, $CHCl_3$–N_2, $CHCl_3$–air, THF-N_2, and THF-air, respectively. Above observations ensure that the following measurements of physical quantities such as dn/dc and adsorption coefficients for PPA polymers can be accurate enough for our purposes.

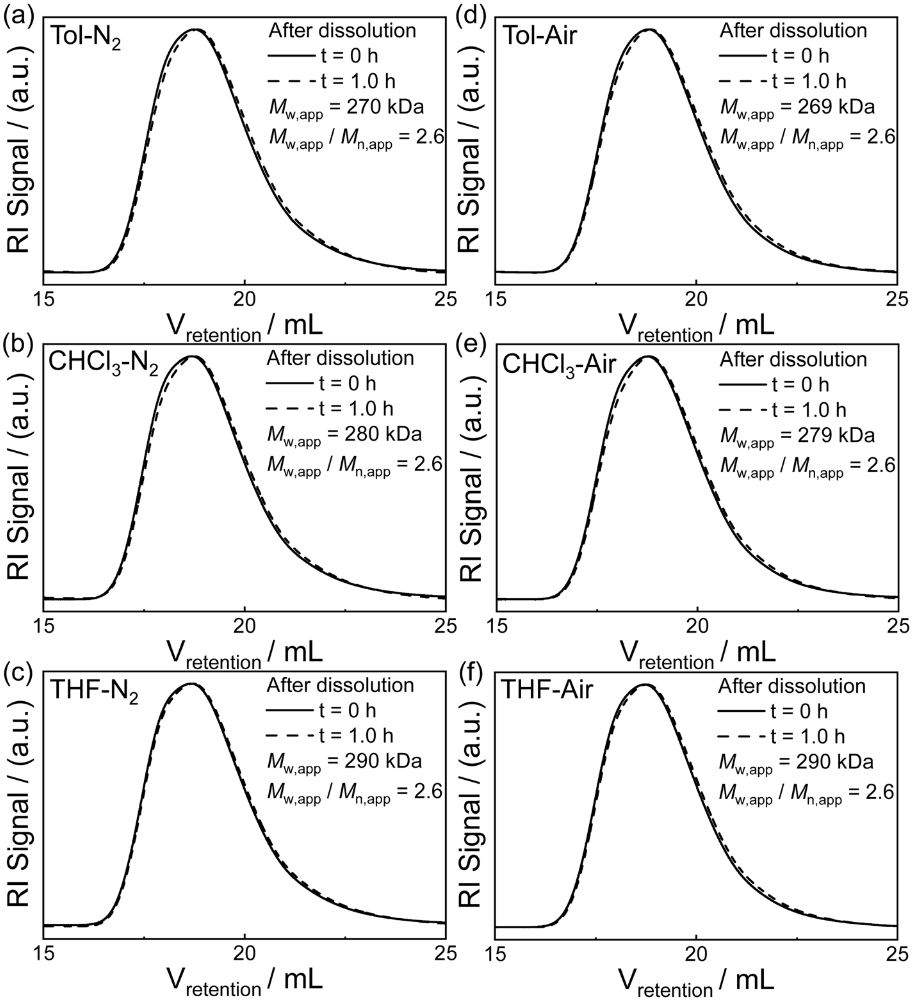

Fig. 1 Size exclusion chromatography (SEC) curves of PPA (solid powder) measured in different solvents at different dissolution times for $t = 0$ and $t = 1.0$ h under N_2 (a–c) and air (d–f) atmospheres, respectively.

The differential refractive index (dn/dc) and UV-vis absorption spectra were systematically characterized. PPA exhibits dn/dc values of 0.175 mL g^{-1} (Tol), 0.235 mL g^{-1} ($CHCl_3$), and 0.175 mL g^{-1} (THF), with complete datasets provided in Fig. S2.† Fig. 2 presents the absorption spectra for PPA in various solvents, where two distinctive absorption peaks can be clearly observed. The first peak, located at $\lambda = 328$ nm, is attributed to the characteristic absorption of the benzene ring. The second peak, located at $\lambda = 390$ nm, is assigned to the characteristic absorption of the conjugated backbone. Significant ultraviolet absorption can be observed in the range of λ from 300–500 nm. Importantly, when $\lambda > 500$ nm, no absorption is observed, which ensures the feasibility of using LLS to investigate the molecular information without the risk of absorption of the incident laser. Moreover, by plotting the absorbance measured at $\lambda = 328$ nm against solution concentration (as shown in Fig. 2d–f), we can determine the molar absorption coefficients of PPA in various solvents, which are useful for the *in situ* estimation of the absolute concentration of PPA during the polymerization, crucial for subsequent analyses.

2.3 Evolution of the SEC curve during the competitive growth-degradation polymerization process

For the polymerization conditions listed in Table 1, SEC was initially employed to monitor the temporal evolution of chain growth-degradation competition over a 200-hour period. Key parameters including apparent molar mass ($M_{\mathrm{w,app}}$), molecular weight distribution, and monomer conversion were systematically analyzed.

Fig. 3 displays SEC elution profiles acquired at progressive time intervals for PPA polymerization mixtures under varying solvent and atmospheric conditions. The chromatograms reveal three distinct time-dependent characteristics.

First, across all reaction conditions, SEC elution signals exhibit a monotonic increase as polymerization progresses from $t = 0$–0.08 h (red curves) to 1.0–2.0 h (blue curves), irrespective of solvent or atmosphere. This universal behavior confirms sustained chain growth during initial polymerization stages, with all systems maintaining monomodal distributions.

Second, beyond $t = 1.0$–2.0 h, chromatograms progressively shift toward higher elution volumes (black → brown curves),

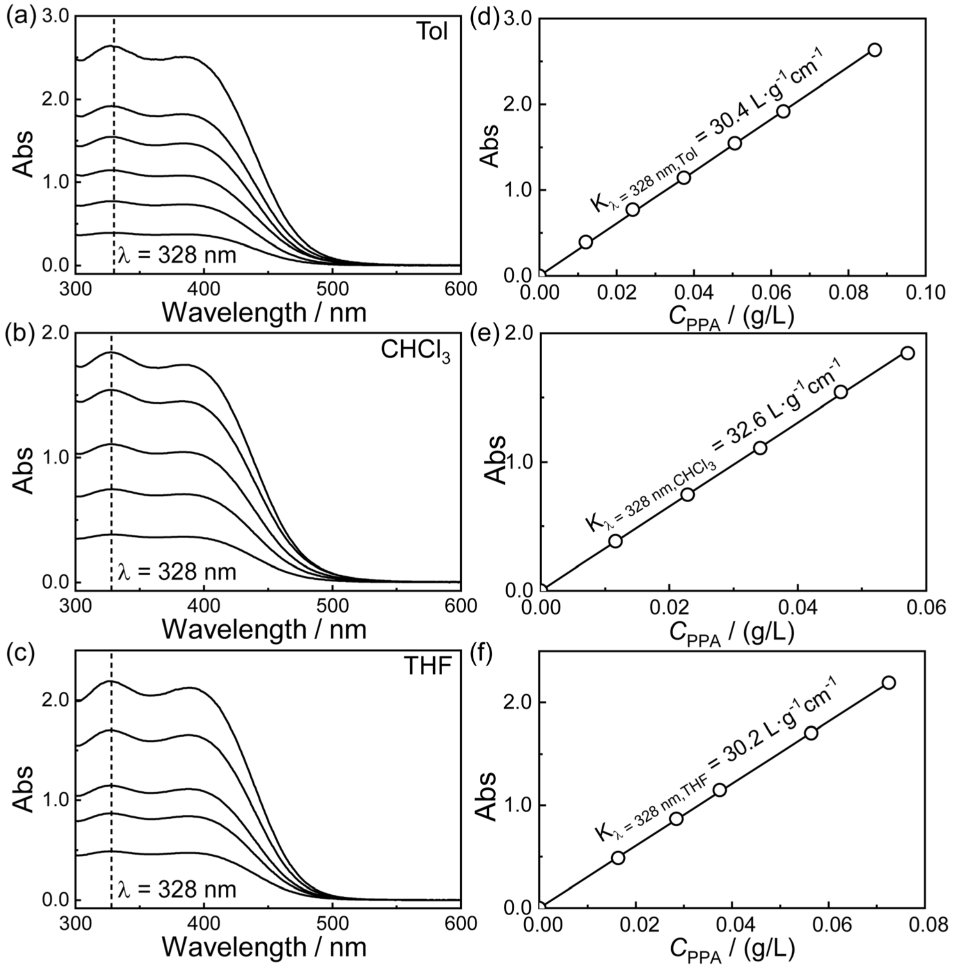

Fig. 2 (a–c) Ultraviolet-visible absorption spectra for PPA in different solvents. (d–f) Solution concentration (C_{PPA}) dependence of absorbance (Abs) for PPA in different solvents.

accompanied by peak broadening and eventual splitting into multiple populations. This progression suggests stochastic chain scission events, generating polydisperse fragments ranging from large macromolecules to oligomers.

Third, comparative analysis of Fig. 3a–c (N_2) *versus* Fig. 3d–f (air) reveals delayed degradation kinetics under inert atmosphere. Quantitative tracking shows polydispersity indices increasing from ∼2.5 to ∼6.0, with $M_{\mathrm{w,app}}$ decreasing from ∼300 kDa to ∼500 Da (elution volume = 27 mL). Fragments below 500 Da (1–5 repeat units) exceed conventional SEC detection limits (Fig. S3†), preventing accurate quantification.

Further, the dependence of $M_{\mathrm{w,app}}$ on polymerization time (t_{p}) is quantitatively analyzed in Fig. 4a and b. Roughly, the $M_{\mathrm{w,app}}$–t_{p} dependence curve can be divided into two stage, *i.e.*, slow and rapid decline region, as indicated by the solid and dashed lines. Clearly, it is reasonable to attribute the slow decline region to the competition between chain growth and degradation in the early stage of the polymerization reaction, which was not clarified in previous studies.[32] Note that such a two-stage feature is universal for different conditions of solvent and atmosphere, but the absolute values and transition regions are significantly different from one experimental condition to another.

Notably, under N_2-THF conditions, an atypical kinetic profile emerges: $M_{\mathrm{w,app}}$ initially increases gradually before subsequent decline. We believe that this observation further supports the competitive process between chain growth and degradation. In the later stage of polymerization, the catalyst loses its activity, which results in the rapid decline in $M_{\mathrm{w,app}}$ because of chain degradation.

We define the transition time (t_{transit}) between kinetic regimes. Under N_2, t_{transit} follows $CHCl_3$ (65 h) > THF (35 h) > Tol (25 h); under air, the order persists but durations shorten to $CHCl_3$ (16 h) > THF (11 h) > Tol (6 h). On the other hand, the order of t_{transit} seems to correlate with solvent property, such as the polarity, dipole moment, viscosity, and interaction parameters, namely, the order of polarity $CHCl_3$ > THF > Tol.

Maximum achievable $M_{\mathrm{w,app}}$ exhibits solvent dependence: THF yields 865 kDa (slow kinetics), whereas Tol and $CHCl_3$ reach 330 kDa and 478 kDa within 0.08 h (Fig. S4†). Post 100–200 h polymerization, $M_{\mathrm{w,app}}$ retains merely 5% of peak values across all systems.

SEC peak area analysis (Fig. 5) reveals triphasic monomer conversion kinetics: The following findings can be highlighted: (1) on the time scale of 10^{-1} h, which is the first point in the figure, a high conversion has been reached, and the peak of the

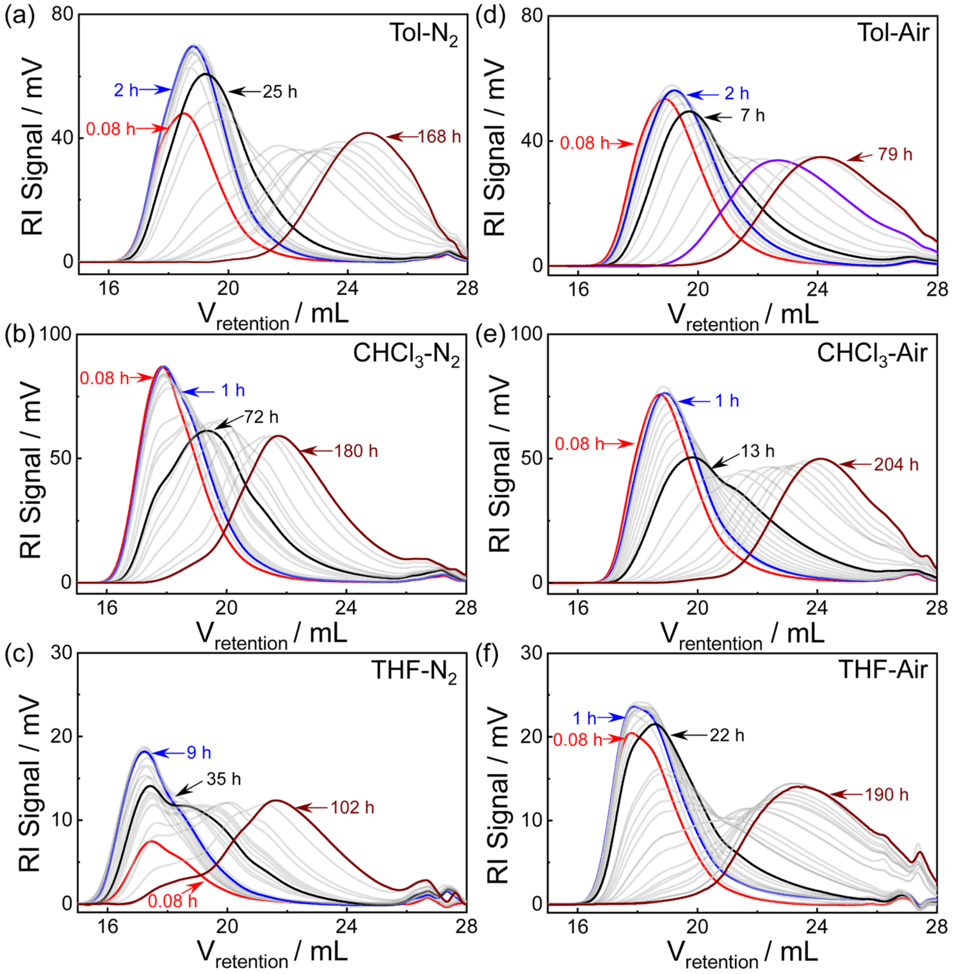

Fig. 3 Size exclusion chromatography (SEC) curves measured at different polymerization times for the mixed solutions in the PPA polymerization systems under different conditions of solvent and atmosphere, (a–c) N_2; (d–f) air. The grey data are SEC curves measured at intermediate time intervals which are not marked in the figure.

slow rising stage corresponds to the maximum conversion of the monomer, and the subsequent decline process is mainly due to the decrease in the size of degraded products, with their molar mass close to the solvent species ($V_{\text{retention}} \approx 27$ mL, M from 100 to 300 Da); (2) under both N_2 and air, the maximum peak areas in different solvents show significant variation. After calculation, $CHCl_3$ gives the highest conversion at around 15%, while THF gives the lowest conversion around 3%; (3) for a given solvent, the difference in conversion is not very significant between N_2 and air systems. In particular, the ranking of conversion in different solvents remains consistent under both N_2 and air atmospheres, namely, $CHCl_3$ > Tol > THF.

Upon normalizing the data in Fig. 5a and b based on conversions measured at $t_p = 0.08$ h, we identified trends in the relative SEC peak areas. The normalized results are shown in Fig. 6a and b. Under N_2, the $t_{\max}$ values in Fig. 6a varied significantly between solvents, reflecting differences in the time scale of monomer-to-polymer conversion processes. Specifically, $t_{\max}$ was approximately 23 h for THF, compared to 2.0–3.0 h for $CHCl_3$ and Tol, indicating much faster kinetics. The maximum conversions in $CHCl_3$ and Tol reached approximately 1.5 times higher than their initial values at $t_p = 0.08$ h, whereas in THF it exceeded three times the initial value. Similar trends were observed under air.

2.4 Evolution of UV-vis spectra during the competitive growth-degradation polymerization process

In addition to SEC, UV-vis spectra of the polymerization system were monitored to trace the evolution of conjugation features. Fig. 7a and b displays the results for PPA-Tol system under different atmospheres. The two characteristic peaks at $\lambda = 328$ and 390 nm are attributed to the conjugated phenyl ring and conjugated carbon backbone, respectively. The peak features remain observable during polymerization but gradually weaken over time, with intensities showing dependence on polymerization time. Fig. 7c and d illustrate how the absorbance (Abs) measured at $\lambda = 328$ and 390 nm changes over time for the PPA-Tol system. Notably, distinct transition behaviors are observed in Abs-t_p plots: at 2.0 h and 30 h under N_2, and 1.5 h and 9.0 h under air. These transition times are significantly longer than those indicated by SEC peak areas, though both show consistent

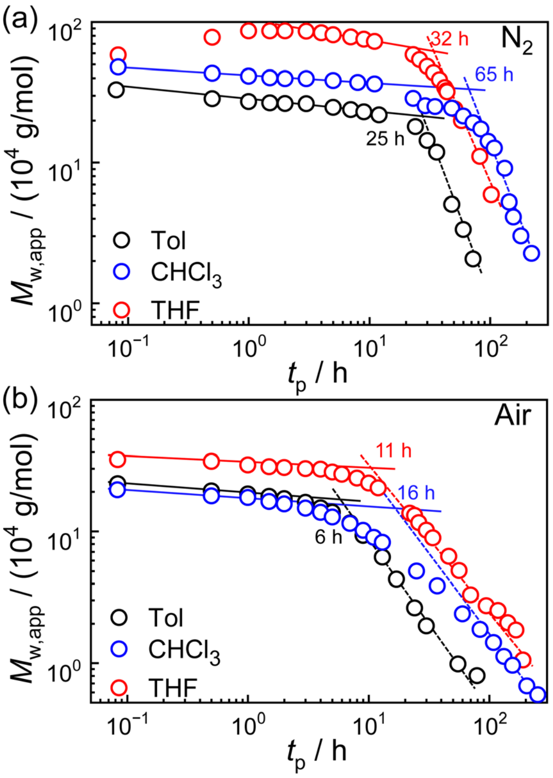

Fig. 4 Polymerization time (t_p) dependence of apparent weight-average molar mass ($M_{w,app}$) measured by size exclusion chromatography (SEC) for PPA in different solvent conditions under (a) N_2 and (b) air.

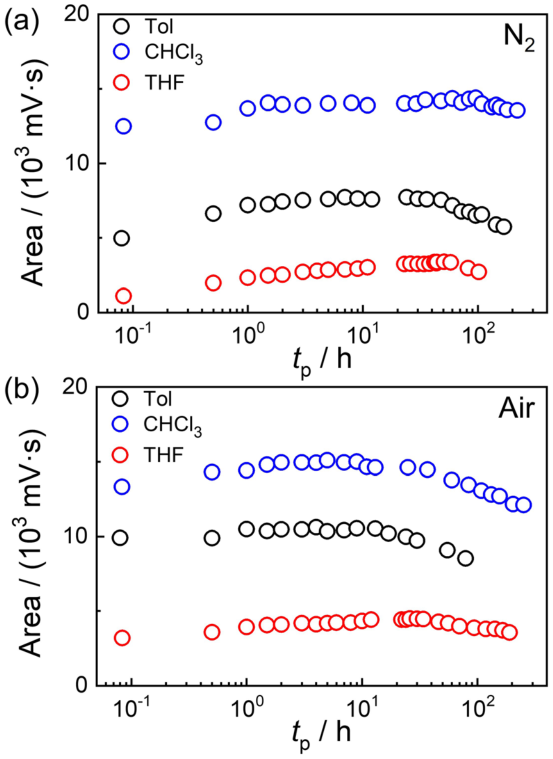

Fig. 5 Polymerization time (t_p) dependence of peak area of SEC curve in different solvents and atmospheres: (a) N_2 and (b) air.

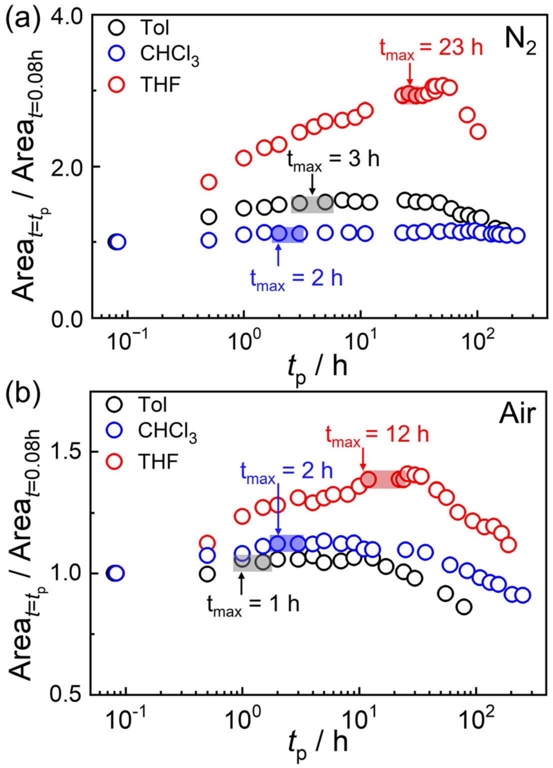

Fig. 6 Polymerization time (t_p) dependence of normalized peak area of size exclusion chromatography (SEC) curve (area $_{t_p=t}$/area$_{t_p=0.08h}$) in different solvents and atmospheres: (a) N_2 and (b) air.

trends. This might involve thermally induced degradation pathways through which molecular conformations undergo *cis–transoid* to *cis–cisoidal* transitions, enhancing conjugation. The time-dependent transition suggests that larger conjugated fragments are primarily formed in earlier stages, while smaller non-conjugated fragments emerge predominantly in later stages, exhibiting clear random degradation characteristics. Similar trends were observed for $CHCl_3$ and THF systems under different atmospheres, as shown in Fig. S5.†

It is also instructive to plot A_{328nm}/A_{390nm} *versus* t in Fig. 7e and f. In the PPA-Tol system (black data), clear transitions occur at $t_p = 30$ h (N_2) and 8.0 h (air), closely matching the transition times in Fig. 7c and d. The increase in A_{328nm}/A_{390nm} reflects a rising mass fraction of non-conjugated components, indicating that chain degradation dominates in later stages rather than polymerization. Specifically, under N_2, transition times for Tol, THF, and $CHCl_3$ were 30 h, 35 h, and 80 h, respectively. Under air, transition times were significantly longer: 8 h (Tol), 18 h (THF), and 28 h ($CHCl_3$), reflecting accelerated degradation kinetics of conjugated segments under oxidative conditions.

2.5 Difference in the absolute and apparent molar masses of PPA chains in solution

Based on the above SEC and UV-vis results, the qualitative effects of solvents and atmospheric conditions on the chain growth-degradation competition have been established. However, SEC only provides relative molar mass values.

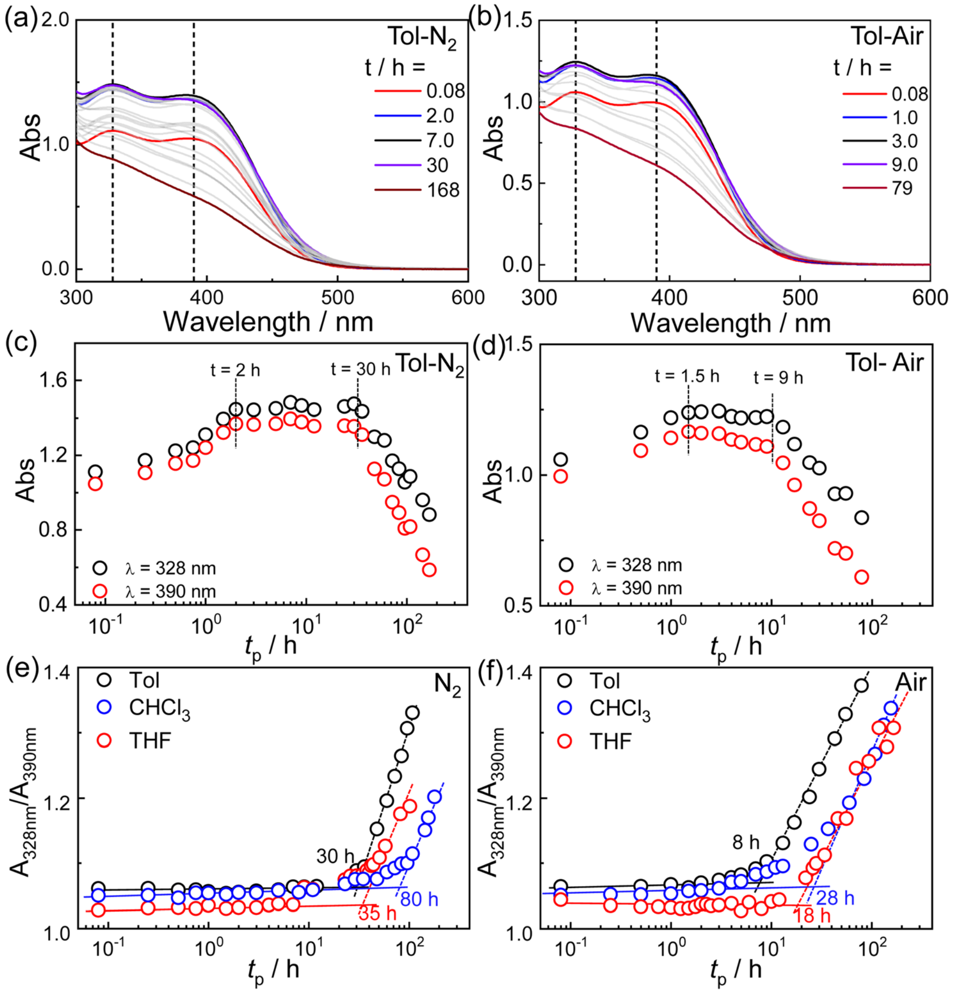

Fig. 7 (a and b) Ultraviolet-visible absorption (UV-vis) spectra for PPA-Tol system measured at different polymerization times (t_p) under different atmospheres. (c and d) Polymerization time (t_p) dependence of absorbance (Abs) for PPA-Tol system under different atmospheres. (e and f) Polymerization time (t_p) dependence of characteristic ratio of A_{328nm}/A_{390nm} for PPA systems under different conditions of solvents and atmospheres.

Obtaining absolute molar mass values for PPA, distinct from apparent values, remains essential for quantitative kinetic analysis. LLS measurements of PPA standard samples in Tol, $CHCl_3$, and THF were performed to determine absolute-to-apparent molar mass ratios and facilitate conversion of literature-reported apparent values to absolute values. Solutions were stirred under N_2 for 2 h to ensure complete dissolution. Thus, the solvent-dependent degradation rate of PPA must be considered.

Fig. 8 shows the Zimm plots for PPA sample in different solvents. The absolute-to-relative molar mass ratios ($M_{w,abs}/M_{w,app}$) are approximately 2.3 for Tol and $CHCl_3$, showing high consistency between these solvents. In THF, the ratio increases to ∼3.3, suggesting weak aggregation of PPA. The observed discrepancy may arise from shear-induced disaggregation during SEC measurements, whereas LLS measurements lack shear forces, preserving aggregated states and yielding higher $M_{w,abs}$ values in THF. This mechanistic hypothesis requires further validation.

Repeated experiments validated the above observations. The results indicate that the absolute weight-average molar mass ($M_{w,abs}$) is significantly higher than $M_{w,app}$ determined *via* SEC with PS standards. This establishes quantitative consistency, enabling conversion of apparent molar mass data to absolute values for broader applicability. However, the marked discrepancy between $M_{w,abs}$ and $M_{w,app}$ raises a critical warning: conclusions based solely on apparent molar mass data may require re-evaluation.

2.6 Degradation kinetics of PPA chains in dilute solutions by LLS

A systematic investigation of PPA chain degradation kinetics in dilute solutions remains critical for three reasons: (1) in polymerization systems with complex compositions and high concentrations, distinguishing the contributions of chain growth and degradation to measured quantities is challenging; (2) shear forces in SEC may disassemble weakly aggregated species, obscuring real aggregation-degradation behavior; (3)

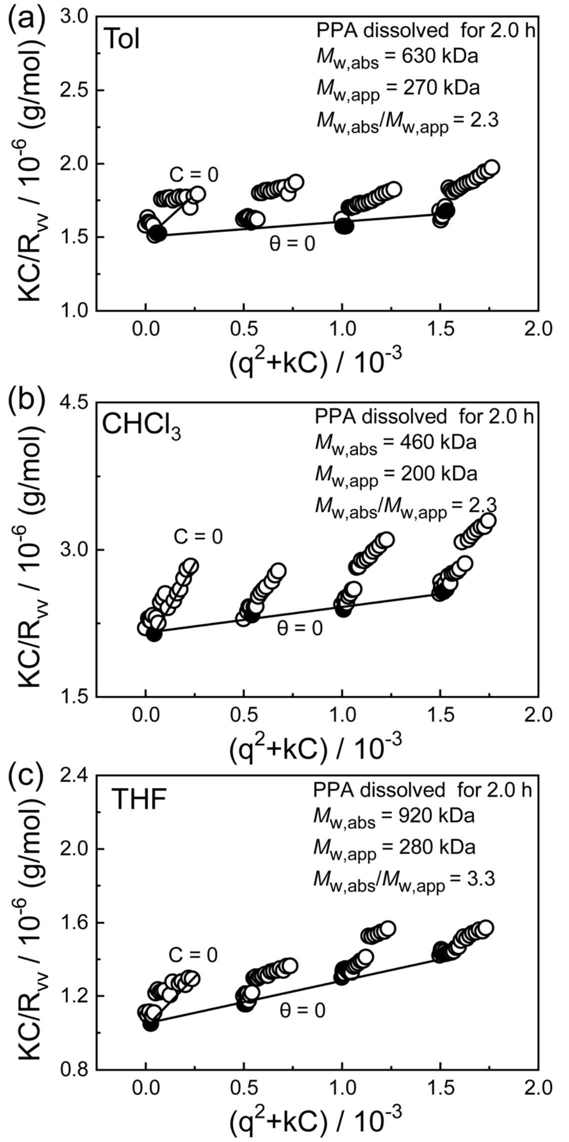

Fig. 8 Zimm plots of PPA powder samples dissolved in (a) toluere, (b) $CHCl_3$ and (c) THF, where all solutions are stirred under N_2 for 2.0 h to ensure the complete dissolution.

prior studies lack systematic characterization of PPA degradation in dilute solutions. To address this, $M_{w,abs}$, $\langle R_g \rangle$, $\langle R_h \rangle$, and $f(R_h)$ were analyzed *via* combined static/dynamic LLS to elucidate degradation mechanisms under dilute conditions.

To monitor the degradation kinetics in dilute solution, it is necessary to confirm the reliability of signal-to-noise ratio of the light intensity, as well as the accuracy of average molar mass, measured at a single concentration. Generally, the scattering intensity of the tested PPA solution should one order of magnitude stronger than the solvent, and the deviation of the molar mass fitted at a specific concentration should be within ±30% when compared with the result fitted at $C = 0$.

As shown in Fig. 9a (Tol), I/I_0 gradually decreases with increasing t_d (0–10 h): from 5.0 to 2.5 ($C = 0.6$ g L^{-1}), 12 to 5.0 (1.2 g L^{-1}), and 18 to 7.0 (1.8 g L^{-1}). Similar trends are observed for $CHCl_3$ (Fig. 9b; 40 → 20 at 1.0 g L^{-1}, 70 → 20 at 2.0 g L^{-1}, 100 → 30 at 3.0 g L^{-1}) and THF (Fig. 9c; 60 → 50 at 1.0 g L^{-1}, 110 → 80 at 2.0 g L^{-1}, 160 → 110 at 3.0 g L^{-1}). These results indicate that concentrations near 1.8 g L^{-1} satisfy signal-to-noise ratio requirements across solvents.

Fig. 9d–f compare $M_{w,abs}$ values from single- and multi-concentration fittings. For Tol and $CHCl_3$, both methods yield comparable results, whereas multi-concentration fitting gives higher $M_{w,abs}$ in THF. Relative deviations between methods (Fig. 9g–i) remain within ±30%, meeting acceptance criteria. Based on scattering intensity and deviation thresholds, 2.0 g L^{-1} was selected for further kinetic studies.

Fig. 10a and b shows how the normalized weight average molar mass of PPA changes with time under N_2 and air. Clearly, a notably faster degradation rate is observed under air, which is qualitatively consistent with the previous observation for the competitive polymerization process. Empirically, the degradation curves can be described by the single-exponential decay model, *i.e.*, $y = Ae^{(-x/t_c)} + (1 - A)$, where t_c is the characteristic decay time. In principle, a smaller t_c means a faster degradation process. Under N_2, t_c follows the order as: $t_{c,Tol} = 17.4 > t_{c,THF} = 14.5 > t_{c,CHCl_3} = 2.8$, while under air, t_c follows the order as: $t_{c,THF} = 10.4 > t_{c,Tol} = 6.4 > t_{c,CHCl_3} = 2.3$. The t_c values measured under N_2 are all greater than those measured under air for a given type of solvent.

In the competition kinetics of degradation and re-aggregation, PPA chains are found to undergo degradation more slowly under N_2 than under air, aligning with previous results of polymerization in concentrated solution. In particular, it is found: (1) in dilute solution, $M_{w,abs}$ decreases fastest with time in $CHCl_3$, followed by Tol, and slowest in THF, which is slightly different from the case in concentrated solution, where $M_{w,app}$ decreases fastest with time in Tol, followed by THF, and slowest in $CHCl_3$; (2) the M_w–t curves generally exhibit a two-stage feature, but in the competition process of growth and degradation, a slow decline is observed at the beginning followed by a fast decline, in contrast for the competition process of degradation and re-aggregation, the order is observed to be reversed due to the lack of chain growth; (3) critically, solvent-dependent degradation rates reverse between systems: Concurrent polymerization exhibits Tol > THF > $CHCl_3$, whereas pure degradation shows THF > Tol > $CHCl_3$. This dramatic reversal stems from polymerization dominance competing with degradation. The underlying solvent effects are elucidated by degradation mechanisms: Under anaerobic conditions (primarily thermal degradation), the rate order THF ≈ Tol << $CHCl_3$ arises from $CHCl_3$'s acid catalysis accelerating steps like cyclization/cleavage, while minimal THF/Tol difference indicates thermal degradation's weak kinetic sensitivity to polarity. Under aerobic conditions (thermal and oxidative degradation), accelerated rates follow $CHCl_3$ >> THF > Tol due to combined acid catalysis and oxidative enhancement the THF > Tol divergence reflects polar solvent stabilization of peroxide intermediates in oxidative degradation.

Thus, for the competition of degradation and re-aggregation in $CHCl_3$, PPA chains display the fastest molar mass change, whereas, for the chain growth and degradation competition, it

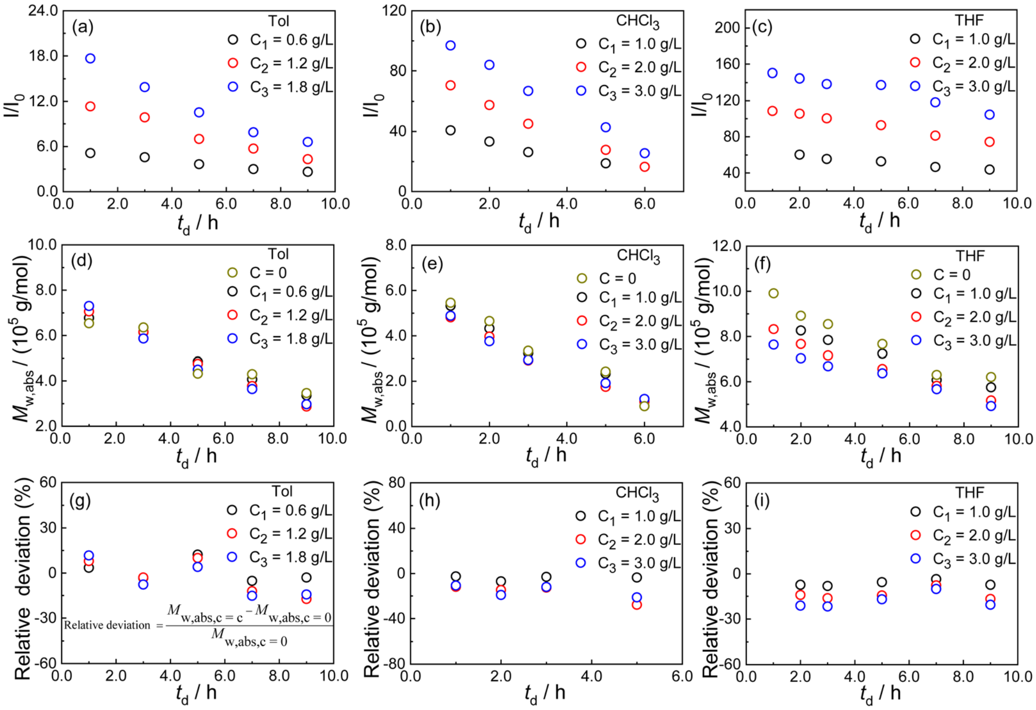

Fig. 9 Degradation time (t_d) dependence of (a–c) relative scattering intensity (I/I_0), (d–f) weight average molar mass ($M_{w,abs}$), and (g–i) the relative deviation of weight average molar mass [$(M_{w,abs,c=c} - M_{w,abs,c=0})/M_{w,abs,c=0}$] for PPA solutions at varied conditions of concentration and solvent.

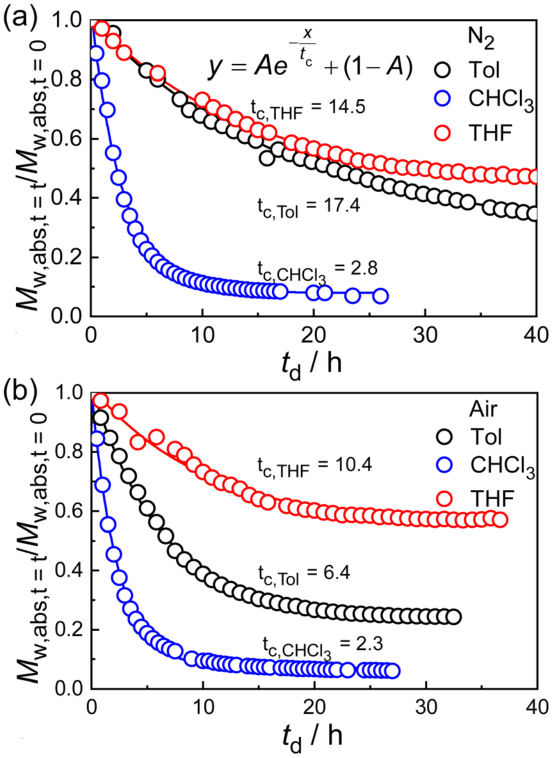

Fig. 10 Degradation time (t_d) dependence of normalized weight average molar mass ($M_{w,abs,t=t}/M_{w,abs,t=0}$) for PPA solutions with C = 2.0 g L^{-1} under different atmospheres: (a) N_2 and (b) air.

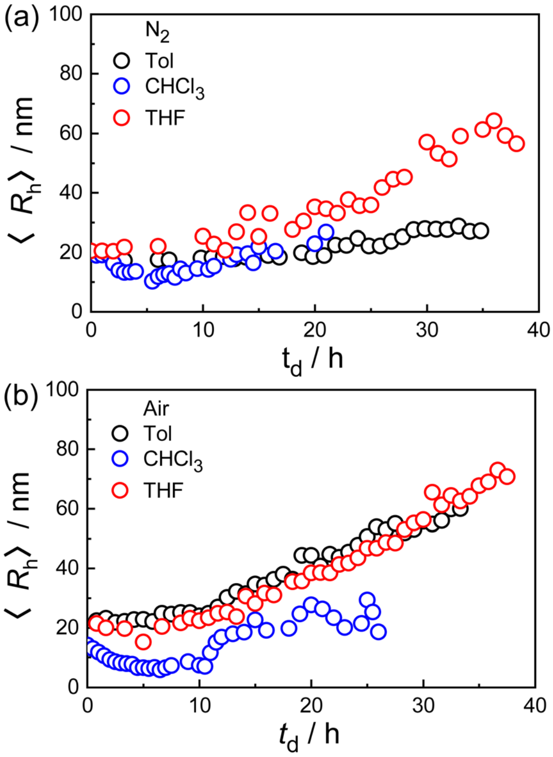

Fig. 11 Degradation time (t_d) dependence of the z-average hydrodynamic radius ($\langle R_h \rangle$) for PPA solutions with C = 2.0 g L^{-1} under different atmospheres: (a) N_2 and (b) air.

is the slowest. This clearly suggests again that, chain growth dominates over degradation in the early stages of polymerization. In $CHCl_3$, as shown in Fig. 4, it takes 65 h under N_2 and 16 h under air to reach the characteristic transition time, which is totally different from Fig. 10 in which the molar mass of PPA chains is found to decrease by over 80% within 16 h both under N_2 and air.

Simultaneously, the z-average hydrodynamic radius, *i.e.*, $\langle R_h \rangle$, is followed as a function of t_d. Interestingly, Fig. 11a and b shows the abnormal and surprising increase in $\langle R_h \rangle$ when $t_d >$ 10 h. The PPA solutions exhibit similar trends for both N_2 and air atmospheres. Specifically, (1) when $t_d < 10$ h, $\langle R_h \rangle$ remains almost unchanged for THF and Tol systems, or slightly decrease for $CHCl_3$ system; (2) when $t_d > 10$ h $\langle R_h \rangle$ starts to gradually increase with time; (3) the differences in $\langle R_h \rangle$ changes under different atmospheres are not significant, and $\langle R_h \rangle$ remain below 100 nm at $t_d = 40$ h. For instance, for $CHCl_3$ solution under air (Fig. 10b), $\langle R_h \rangle$ decreases from 14 to 6.0 nm within the first 6.0 h, and then increases from 6.0 to 25 nm over the next 19 h, and the rate of decrease in size is more pronounced when compared with Tol and THF. How to rationalize such an abnormal and surprising observation for the invers trends of $\langle R_h \rangle$ and $M_{w,abs}$?

Intuitively, we hypothesize the main reason to be the competition between chain degradation and re-aggregation during the degradation process. Namely, the PPA chains can undergo chain degradation in the initial stage, which results in the formation of much smaller segment fragments, but in the later stage, these fragments are still possible to undergo the re-aggregation to form much larger aggregates *via* intermolecular interactions such as π–π stacking. This is because the degradation fragments may possess different chemical compositions according to the heat- and oxygen-induced degradation pathways, which can potentially result in the change of polymer–solvent interactions.

To confirm our hypothesis, the hydrodynamic radius distribution, *i.e.*, $f(R_h)$, is further analyzed in Fig. 12. The trends are generally consistent across all solvent and atmosphere systems, namely, (1) initially at $t_d = 0$, a set of main peak located from 8–20 nm is observed for PPA individual chains, in addition, the air-THF and air-Tol systems give an extra small peak located around 100–200 nm, indicating the existence of trace amount of aggregates under air system; (2) when 0 h < t_d < 30 h, the main peak of $f(R_h)$ is found to gradually split into multi-peaks over time for all systems, signifying the simultaneous formation of both smaller fragments and larger aggregates; (3) in the end, the

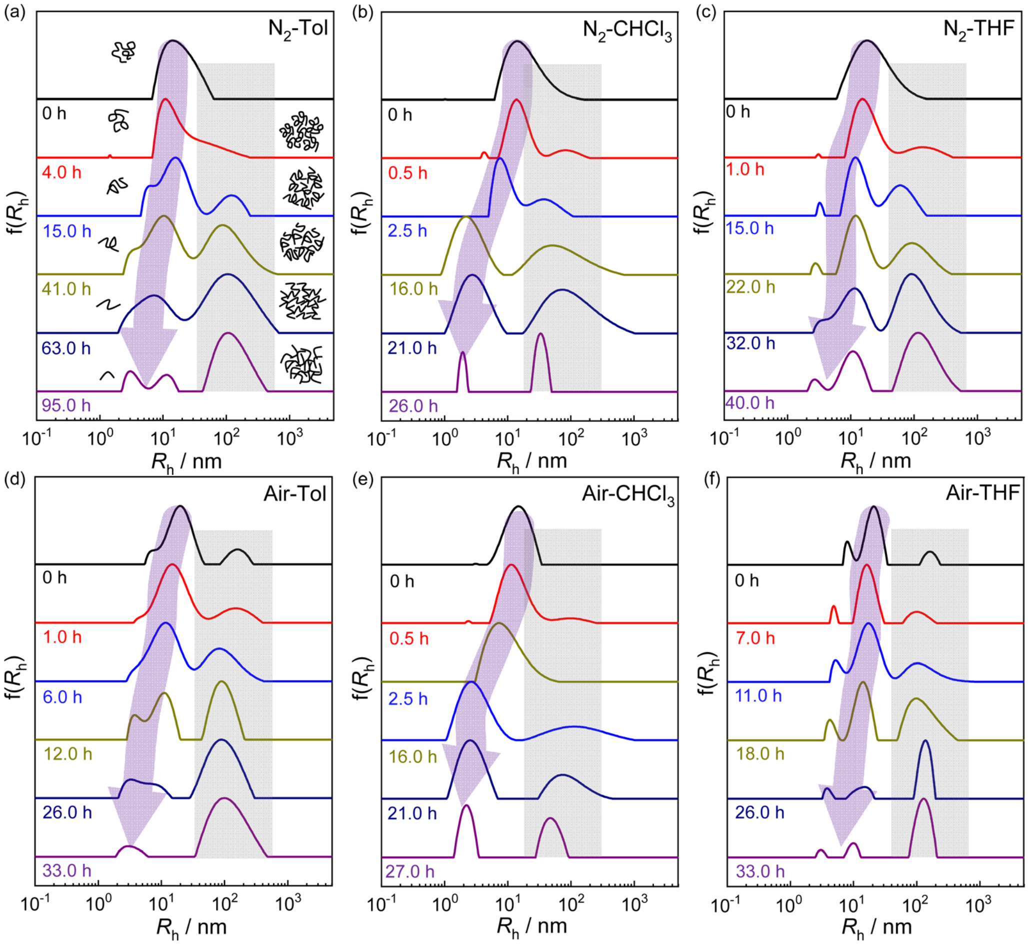

Fig. 12 Degradation time (t_d) dependence of hydrodynamic radius distribution [$f(R_h)$] for PPA solutions with $C = 2.0$ g L^{-1} under different atmospheres: (a–c) N_2; (d–f) air.

smaller fragments are found to locate at 2.0–3.0 nm, and the larger aggregates are found to locate around 80–200 nm, if we consider the uncertainty of DLS fitting in the multipeak; (4) the peak areas of smaller fragments and large aggregates both continuously increase with time. Specifically, under N_2, the peak splitting starts at $t_d = 0.5$ h, 4.0 h and 1.0 h for $CHCl_3$, Tol and THF, respectively. While under air, the peak splitting is observed to occur at $t_d = 0.5$ h for all three solvent system, mainly due to the faster degradation kinetics under air. Note that unlike Tol and THF systems, almost no aggregates are observed at $t_d = 0$ h for $CHCl_3$ system, this correlates with the evolution of $\langle R_h \rangle$ in Fig. 11. In fact, the degradation and aggregation occur simultaneously and more significantly in Tol and THF, which can result in less pronounced reduction in $\langle R_h \rangle$. In contrast, PPA in $CHCl_3$ shows a more significant reduction in $\langle R_h \rangle$ mainly due to degradation without aggregation at the early stage. We should admit that the aggregates can be a mixture of linear, hyperbranched and spheric species.

Overall, the result in Fig. 12 not only supports our hypothesis, but also rationally explains the observations in Fig. 10 and 11 for the evolution of molar mass and chain size. On the other hand, we note that above phenomenon was not observed in the SEC in Fig. 3–6, which is probably due to the existence of flow field in SEC, which provides external disturbance to disrupt aggregates with weak interactions, which is to be studied in detail in future work.

3 Conclusion

In this study, we revealed the competitive kinetics of chain growth, degradation, and re-aggregation during the Rh-catalyzed polymerization of PA. Our key findings include: (1) a universal two-stage degradation behavior in the $M_{w,app}$–t_p dependence was observed. Initially, a slow degradation dominated, driven by the competition between growth and degradation. As polymerization continued, catalyst deactivation led to a rapid decrease in $M_{w,app}$, indicating degradation dominance. Transition time and maximum molar mass were significantly influenced by solvent and atmosphere. (2) UV-vis and SEC analyses revealed that conversion and degradation kinetics varied with solvent, with $CHCl_3$ achieving the highest conversion and THF the lowest. Faster kinetics were observed under air compared to nitrogen, emphasizing the impact of oxidative conditions. (3) The ratio of $M_{w,abs}$ to $M_{w,app}$ for PPA, determined by LLS, ranged from 2.3 to 3.3 across solvents, providing a method to convert apparent mass data into more accurate absolute values. (4) In dilute solutions, degradation was slower under N_2 than under air, consistent with our concentrated solution findings. $CHCl_3$ exhibited the fastest degradation, followed by toluene and THF. (5) During degradation, an initial breakdown of PPA chains into smaller fragments was followed by re-aggregation into larger aggregates. Peak splitting times varied by solvent and atmosphere, with air inducing earlier and more significant degradation. These findings deepen our understanding of the complex interplay between solvent properties, atmospheric conditions, and polymer chain dynamics, offering valuable insights for further optimizing polymerization processes and improving the stability of conjugated polymers.

4 Experimental section

4.1 Materials

Phenylacetylene (PA, Macklin, 97%) was distilled under reduced pressure after drying over CaH_2 for 24 h (Sinopharm, 99.5%). Triethylamine (Et_3N, energy chemical, 99%), tetrahydrofuran (THF, Meryer, 99%), and toluene (Tol, Sinopharm, AR) were distilled after drying over CaH_2 for 24 h. Chloroform ($CHCl_3$, Sinopharm, AR) was purified prior to use, by extracting three times with ultrapure water to remove the stabilizer, and then distilling after drying with anhydrous magnesium sulfate. $[Rh(nbd)Cl_2]_2$ (Eybridge, 97%) and other chemicals were used as received.

4.2 Experiment

In a typical experiment, the catalyst $[Rh(nbd)Cl_2]_2$ (7.21 mg, 0.016 mmol), co-catalyst Et_3N (4.0 μL, 0.032 mmol), and Tol (30 mL) were added into a dried round-bottom flask. Subsequently, 20 mL Tol solution containing PA (3.2 g, 31.3 mmol) was rapidly injected into the round-bottom flask under stirring at 25 °C. After stirring for predetermined time interval, 100 μL sample solution was taken out and diluted for 3 times. The diluted sample solution was used for the subsequent tests.

4.3 Size exclusion chromatography (SEC)

The SEC system consists of a P98II constant volume HPLC pump, an automatic sampler, and an RI detector (Shodex RI-201H, $T = 35$ °C). Employed in this system are three Shodex columns (KF-802.5, KF-804, and KF-806). Eluent THF was used with a flow rate of 1.0 mL min^{-1}. The apparent number-average molar mass ($M_{n,app}$), apparent weight-average molar mass ($M_{w,app}$), and apparent peak molar mass ($M_{p,app}$) of the relevant samples were determined using narrowly distributed PS samples as calibration standards. Prior to injection, all sample solutions were filtered through PTFE membranes with a 0.22 μm pore size.

4.4 Ultraviolet-visible spectroscopy (UV-vis)

In a typical experiment, 100 μL of the PPA solution was withdrawn and diluted to 10 mL. Subsequently, 500 μL of this dilution was taken and further diluted to 5 mL. The UV-vis absorption spectra of the PPA solution, ranging from 200 nm to 700 nm, were recorded using a GENESYS 50 UV-vis Spectrophotometer (Thermo Fisher Scientific) in a 1 cm path-length quartz cuvette, with the pure solvent as the background.

4.5 Measurement of the differential refractive index (dn/dC)

The differential refractive index was measured as follows: Poly(phenylacetylene) (PPA, 2.0 g) was dissolved in toluene (Tol, 30.0 g), centrifuged, and the supernatant filtered through a 0.45 μm membrane (Millipore). A 25.0 g aliquot of the filtrate was rotary-evaporated to dryness for gravimetric determination of soluble

PPA concentration. The remaining solution (1 g) was diluted to 30 g with toluene to form a stock solution, which was then serially diluted to yield five concentrations for dn/dC measurement; aqueous sodium chloride (NaCl) solutions of varying concentrations served as calibration standards. Solutions were infused into a refractive index detector (Waters 2414) *via* a gas-tight syringe and Luer-lock fittings using a programmable syringe pump (flow rate: 1.0 mL min^{-1}), and the signal was recorded. Concentrations were converted from g g^{-1} to g mL^{-1} using solvent density. The dn/dC value for NaCl, derived from the slope of the refractive index signal *versus* concentration (g mL^{-1}) plot, was used to calibrate the instrument constant. The dn/dC of PPA in toluene was then determined analogously. A similar methodology was employed for PPA in $CHCl_3$ and THF.

4.6 Static light scattering (SLS)

This study employs a commercial light scattering (LS) spectrometer (ALV/CGS-3) equipped with a multi-digital time correlator (ALV-7004) (ALV Co, Germany). In SLS, the absolute excess time-averaged scattering intensity (Rayleigh ratio $R_{vv}(q)$), the absolute weight-average molar mass ($M_{w,abs}$) root-mean-square radius of gyration ($\langle R_g \rangle$), and second virial coefficient (A_2) can be determined based on their angular dependence using eqn (1).

$$\frac{KC}{R_{vv}(q)} = \frac{1}{M_w}\left(1 + \frac{1}{3}\langle {R_g}^2 \rangle q^2\right) + 2A_2C \tag{1}$$

where $q=(4\pi n/\lambda_0)\sin(\theta/2)$, $K = 4\pi 2n(\mathrm{d}n/\mathrm{d}c)^2/(\mathrm{N_A}{\lambda_0}^4)$, Here, λ_0 is the wavelength of light in a vacuum, and N_A is Avogadro's number. Data fitting was performed using the Zimm plot. In the SLS measurements, the concentration range of the PPA solution was 1.0–3.0 g L^{-1}.

4.7 SLS sample preparation

PPA synthesized over 1 h was purified and vacuum-dried to yield a powder. The powder was dissolved in selected solvents under ambient air or nitrogen atmospheres. All solution concentrations were less than one-tenth of the overlap concentration (c^*). Prior to measurement, all solutions were filtered through 0.45-μm PTFE membranes (Millipore) into sample vials and subsequently transferred into quartz light scattering cells.

4.8 SLS measurement

PPA solutions with concentrations ranging from 1.0 to 3.0 g L^{-1} were measured. Static data for one concentration were rapidly acquired at scattering angles (θ) from 21° to 145° (measurement time per concentration <10 min). The remaining two concentrations were then measured sequentially. Thus, static data for all three concentrations were obtained within half an hour. The data were processed using Zimm plots to determine $M_{w,abs}$ and R_g.

4.9 Dynamic light scattering (DLS)

In DLS, the intensity–intensity time correlation function $G^{(2)}(q,t)$,measured in the self-beating mode, can be transformed into the linewidth distribution $G(\Gamma)$ through Laplace inversion, where q is the scattering vector. The translational diffusion coefficient distribution $G(D)$ is obtained using the relationship $\Gamma = Dq^2$. The hydrodynamic radius distribution ($f(R_h)$) is then derived from the Stokes–Einstein equation, $R_h=(k_BT/6\pi\eta_0)/D$,where R_h is hydrodynamic radius, k_B is the Boltzmann constant, T is the absolute temperature, and η_0 is the solvent viscosity. During the DLS measurements, $f(R_h)$ and $\langle R_h \rangle$, as well as the scattering intensity I, were recorded at a scattering angle of 16°.

4.10 SLS measurement

To monitor degradation kinetics in dilute solution, the reliability of the light intensity signal-to-noise ratio and the accuracy of the average molecular weight determined at a single concentration must be confirmed. The general requirements are: (1) the scattered light intensity of the measured PPA solution should be at least one order of magnitude higher than that of the solvent, and (2) the molecular weight obtained by fitting at a specific concentration should deviate by no more than ±30% from the value obtained by extrapolation to zero concentration ($C = 0$). For the three solvents used in this study, the deviations generally fell within ±30%, meeting the criteria.

Therefore, considering the relative deviations in both scattered intensity and molecular weight, a sample concentration of 2.0 g L^{-1} was selected for DLS to investigate the degradation kinetics in dilute solution. Measurements were performed with the cell thermostatted at 25.0 ± 0.1 °C in a toluene bath. R_h, $f(R_h)$ and I were recorded at $\theta = 16°$.

Data availability

All data generated or analyzed during this study are included in this published article and its ESI files.†

Conflicts of interest

The authors declare no conflict of interests.

Acknowledgements

The National Natural Science Foundation of China (22322303 and 22203054), and the Natural Science Foundation for Distinguished Young Scholars of Guangdong Province (2023B1515020001) are gratefully acknowledged.

References

1 J. Liu, J. W. Y. Lam and B. Z. Tang, Acetylenic Polymers: Syntheses, Structures, and Functions, *Chem. Rev.*, 2009, **109**(11), 5799–5867.

2 H. Dong and W. Hu, Multilevel Investigation of Charge Transport in Conjugated Polymers, *Acc. Chem. Res.*, 2016, **49**(11), 2435–2443.

3 G. Li, W.-H. Chang and Y. Yang, Low-bandgap conjugated polymers enabling solution-processable tandem solar cells, *Nat. Rev. Mater.*, 2017, **2**(8), 17043.

4 L. Ding, Z.-D. Yu, X.-Y. Wang, Z.-F. Yao, Y. Lu, C.-Y. Yang, J.-Y. Wang and J. Pei, Polymer Semiconductors: Synthesis, Processing, and Applications, *Chem. Rev.*, 2023, **123**(12), 7421–7497.

5 P. Li, W. Sun, J. Li, J.-P. Chen, X. Wang, Z. Mei, G. Jin, Y. Lei, R. Xin, M. Yang, J. Xu, X. Pan, C. Song, X.-Y. Deng, X. Lei, K. Liu, X. Wang, Y. Zheng, J. Zhu, S. Lv, Z. Zhang, X. Dai and T. Lei, N-type semiconducting hydrogel, *Science*, 2024, **384**(6695), 557–563.

6 T. Zhu, Y. Ni, G. M. Biesold, Y. Cheng, M. Ge, H. Li, J. Huang, Z. Lin and Y. Lai, Recent advances in conductive hydrogels: classifications, properties, and applications, *Chem. Soc. Rev.*, 2023, **52**(2), 473–509.

7 S. Bauer and M. Kaltenbrunner, Semiconductors that stretch and heal, *Nature*, 2016, **539**(7629), 365–367.

8 Y. Zheng, S. Zhang, J. B. H. Tok and Z. Bao, Molecular Design of Stretchable Polymer Semiconductors: Current Progress and Future Directions, *J. Am. Chem. Soc.*, 2022, **144**(11), 4699–4715.

9 W. Wang, Y. Jiang, D. Zhong, Z. Zhang, S. Choudhury, J.-C. Lai, H. Gong, S. Niu, X. Yan, Y. Zheng, C. C. Shih, R. Ning, Q. Lin, D. Li, Y.-H. Kim, J. Kim, Y.-X. Wang, C. Zhao, C. Xu, X. Ji, Y. Nishio, H. Lyu, J. B. H. Tok and Z. Bao, Neuromorphic sensorimotor loop embodied by monolithically integrated, low-voltage, soft e-skin, *Science*, 2023, **380**(6646), 735–742.

10 G. Zhang, Z.-A. Lan and X. Wang, Conjugated Polymers: Catalysts for Photocatalytic Hydrogen Evolution, *Angew. Chem., Int. Ed.*, 2016, **55**(51), 15712–15727.

11 C. Han, S. Xiang, S. Jin, C. Zhang and J.-X. Jiang, Rational Design of Conjugated Microporous Polymer Photocatalysts with Definite D–π–A Structures for Ultrahigh Photocatalytic Hydrogen Evolution Activity under Natural Sunlight, *ACS Catal.*, 2023, **13**(1), 204–212.

12 D. Zhu, Y. Chen, Y. Zhu, C.-Y. Liu, Q. Yan, X. Wu, K. Ling, X. Zhang, P. M. Ajayan, T. P. Senftle and R. Verduzco, Versatile Metal-Free Photocatalysts Based on 3D Covalent Organic Frameworks Capable of Reductive and Oxidative Organic Transformations and Polymerizations, *Macromolecules*, 2024, **57**(3), 1038–1049.

13 A. Jati, S. Dam, S. Kumar, K. Kumar and B. Maji, A π-conjugated covalent organic framework enables interlocked nickel/photoredox catalysis for light-harvesting cross-coupling reactions, *Chem. Sci.*, 2023, **14**(32), 8624–8634.

14 Z. Xu, H. Tsai, H.-L. Wang and M. Cotlet, Solvent Polarity Effect on Chain Conformation, Film Morphology, and Optical Properties of a Water-Soluble Conjugated Polymer, *J. Phys. Chem. B*, 2010, **114**(36), 11746–11752.

15 B. Louis, S. Caubergh, P.-O. Larsson, Y. Tian and I. G. Scheblykin, Light and oxygen induce chain scission of conjugated polymers in solution, *Phys. Chem. Chem. Phys.*, 2018, **20**(3), 1829–1837.

16 S. Oh and E. E. Stache, Recent advances in oxidative degradation of plastics, *Chem. Soc. Rev.*, 2024, **53**(14), 7309–7327.

17 M. Manceau, E. Bundgaard, J. E. Carlé, O. Hagemann, M. Helgesen, R. Søndergaard, M. Jørgensen and F. C. Krebs, Photochemical stability of π-conjugated polymers for polymer solar cells: a rule of thumb, *J. Mater. Chem.*, 2011, **21**(12), 4132–4141.

18 Z.-X. Liu, Z.-P. Yu, Z. Shen, C. He, T.-K. Lau, Z. Chen, H. Zhu, X. Lu, Z. Xie, H. Chen and C.-Z. Li, Molecular insights of exceptionally photostable electron acceptors for organic photovoltaics, *Nat. Commun.*, 2021, **12**(1), 3049.

19 Q. Shen, Y. Cao, S. Liu, M. L. Steigerwald and X. Guo, Conformation-Induced Electrostatic Gating of the Conduction of Spiropyran-Coated Organic Thin-Film Transistors, *J. Phys. Chem. C*, 2009, **113**(24), 10807–10812.

20 O. R. Yamilova, I. V. Martynov, A. S. Brandvold, I. V. Klimovich, A. H. Balzer, A. V. Akkuratov, I. E. Kusnetsov, N. Stingelin and P. A. Troshin, What is Killing Organic Photovoltaics: Light-Induced Crosslinking as a General Degradation Pathway of Organic Conjugated Molecules, *Adv. Energy Mater.*, 2020, **10**(7), 1903163.

21 I. V. Martynov, L. N. Inasaridze and P. A. Troshin, Resist or Oxidize: Identifying Molecular Structure–Photostability Relationships for Conjugated Polymers Used in Organic Solar Cells, *ChemSusChem*, 2022, **15**(3), e202101336.

22 M. Xie, Y. Hua, D. Hong, S. Wan and Y. Tian, Physical insights into protection effect of conjugated polymers by natural antioxidants, *RSC Adv.*, 2021, **11**(3), 1614–1622.

23 D. T. Tran, A. Gumyusenge, X. Luo, M. Roders, Z. Yi, A. L. Ayzner and J. Mei, Effects of Side Chain on High Temperature Operation Stability of Conjugated Polymers, *ACS Appl. Polym. Mater.*, 2020, **2**(1), 91–97.

24 B. X. Dong, C. Nowak, J. W. Onorato, T. Ma, J. Niklas, O. G. Poluektov, G. Grocke, M. F. DiTusa, F. A. Escobedo, C. K. Luscombe, P. F. Nealey and S. N. Patel, Complex Relationship between Side-Chain Polarity, Conductivity, and Thermal Stability in Molecularly Doped Conjugated Polymers, *Chem. Mater.*, 2021, **33**(2), 741–753.

25 S. Riera-Galindo, M. Sanz-Lleó, E. Gutiérrez-Fernández, N. Ramos, M. Mas-Torrent, J. Martín, L. López-Mir and M. Campoy-Quiles, High Polymer Molecular Weight Yields Solar Cells with Simultaneously Improved Performance and Thermal Stability, *Small*, 2024, **20**(26), 2311735.

26 Y.-C. Li, C.-Y. Chen, Y.-X. Chang, P.-Y. Chuang, J.-H. Chen, H.-L. Chen, C.-S. Hsu, V. A. Ivanov, P. G. Khalatur and S.-A. Chen, Scattering Study of the Conformational Structure and Aggregation Behavior of a Conjugated Polymer Solution, *Langmuir*, 2009, **25**(8), 4668–4677.

27 Z.-F. Yao, J.-Y. Wang and J. Pei, Controlling morphology and microstructure of conjugated polymers *via* solution-state aggregation, *Prog. Polym. Sci.*, 2023, **136**, 101626.

28 Y.-C. Li, K.-B. Chen, H.-L. Chen, C.-S. Hsu, C.-S. Tsao, J.-H. Chen and S.-A. Chen, Fractal Aggregates of Conjugated Polymer in Solution State, *Langmuir*, 2006, **22**(26), 11009–11015.

29 R. Noriega, J. Rivnay, K. Vandewal, F. P. V. Koch, N. Stingelin, P. Smith, M. F. Toney and A. Salleo, A general relationship between disorder, aggregation and charge transport in conjugated polymers, *Nat. Mater.*, 2013, **12**(11), 1038–1044.

30 Z. Ke, S. Abe, T. Ueno and K. Morokuma, Rh-Catalyzed Polymerization of Phenylacetylene: Theoretical Studies of the Reaction Mechanism, Regioselectivity, and Stereoregularity, *J. Am. Chem. Soc.*, 2011, **133**(20), 7926–7941.

31 T. Taniguchi, T. Yoshida, K. Echizen, K. Takayama, T. Nishimura and K. Maeda, Facile and Versatile Synthesis of End-Functionalized Poly(phenylacetylene)s: A Multicomponent Catalytic System for Well-Controlled Living Polymerization of Phenylacetylenes, *Angew. Chem., Int. Ed.*, 2020, **59**(22), 8670–8680.

32 K. Echizen, T. Taniguchi, T. Nishimura and K. Maeda, Well-Controlled Living Polymerization of Phenylacetylenes in Water: Synthesis of Water-Soluble Stereoregular Telechelic Poly(phenylacetylene)s, *Angew. Chem., Int. Ed.*, 2022, **61**(26), e202202676.

33 K. Echizen, T. Taniguchi, T. Nishimura and K. Maeda, Synthesis of Stereoregular Telechelic Poly(phenylacetylene) s: Facile Terminal Chain-End Functionalization of Poly(phenylacetylene)s by Terminative Coupling with Acrylates and Acrylamides in Rhodium-Catalyzed Living Polymerization of Phenylacetylenes, *J. Am. Chem. Soc.*, 2021, **143**(9), 3604–3612.

34 K. Cobos, R. Rodríguez, E. Quiñoá, R. Riguera and F. Freire, From Sergeants and Soldiers to Chiral Conflict Effects in Helical Polymers by Acting on the Conformational Composition of the Comonomers, *Angew. Chem., Int. Ed.*, 2020, **59**(52), 23724–23730.

35 E. Suárez-Picado, E. Quiñoá, R. Riguera and F. Freire, Chiral Overpass Induction in Dynamic Helical Polymers Bearing Pendant Groups with Two Chiral Centers, *Angew. Chem., Int. Ed.*, 2020, **59**(11), 4537–4543.

36 F. Freire, J. M. Seco, E. Quiñoá and R. Riguera, Nanospheres with Tunable Size and Chirality from Helical Polymer–Metal Complexes, *J. Am. Chem. Soc.*, 2012, **134**(47), 19374–19383.

37 L. Ren, X. Lu, W. Li, J. Yan, A. K. Whittaker and A. Zhang, Thermoresponsive Helical Dendronized Poly(phenylacetylene)s: Remarkable Stabilization of Their Helicity *via* Photo-Dimerization of the Dendritic Pendants, *J. Am. Chem. Soc.*, 2023, **145**(45), 24906–24921.

38 Y. Cao, L. Ren, Y. Zhang, X. Lu, X. Zhang, J. Yan, W. Li, T. Masuda and A. Zhang, Remarkable Effects of Anions on the Chirality of Thermoresponsive Helical Dendronized Poly(phenylacetylene)s, *Macromolecules*, 2021, **54**(16), 7621–7631.

39 S. M. A. Karim, R. Nomura and T. Masuda, Degradation behavior of stereoregular *cis*–transoidal poly(phenylacetylene)s, *J. Polym. Sci., Part A: Polym. Chem.*, 2001, **39**(18), 3130–3136.

40 T. Masuda, B. Z. Tang, T. Higashimura and H. Yamaoka, Thermal degradation of polyacetylenes carrying substituents, *Macromolecules*, 1985, **18**(12), 2369–2373.

41 D. Bondarev, J. Zedník, I. Plutnarová, J. Vohlídal and J. Sedláček, Molecular weight and configurational stability of poly[(fluorophenyl)acetylene]s prepared with metathesis and insertion catalysts, *J. Polym. Sci., Part A: Polym. Chem.*, 2010, **48**(19), 4296–4309.

42 O. Trhlíková, J. Zedník, J. Vohlídal and J. Sedláček, Molecular weight and configurational stability of poly(phenylacetylene) prepared with Rh catalyst, *Polym. Degrad. Stab.*, 2011, **96**(7), 1310–1320.

43 C. Cametti, P. Codastefano, R. D'Amato, A. Furlani and M. V. Russo, Static and dynamic light scattering measurements of polyphenylacetylene (PPA) in different organic solvents (tetrahydrofuran, toluene and chloroform), *Synth. Met.*, 2000, **114**(2), 173–179.

44 C. Cametti, R. D'Amato, A. Furlani and M. V. Russo, Dynamic light scattering and optical absorption study of poly(monosubstituted)acetylene polymers and copolymers, *Chem. Phys. Lett.*, 2003, **370**(5), 602–608.

45 V. Percec and J. G. Rudick, Independent Electrocyclization and Oxidative Chain Cleavage along the Backbone of *cis*-Poly(phenylacetylene), *Macromolecules*, 2005, **38**(17), 7241–7250.

46 V. Percec, J. G. Rudick, P. Nombel and W. Buchowicz, Dramatic decrease of the *cis* content and molecular weight of *cis*–transoidal polyphenylacetylene at 23 °C in solutions prepared in air, *J. Polym. Sci., Part A: Polym. Chem.*, 2002, **40**(19), 3212–3220.

47 I. Saeed, M. Shiotsuki and T. Masuda, Remarkable Cocatalytic Effect of Alkali Metal Amides and Alkoxides in the Rhodium-Catalyzed Polymerization of Phenylacetylene, *Macromolecules*, 2006, **39**(16), 5347–5351.

48 Y. W, T. M, K. S, Y. K and S. A, Synthesis of Ultra-High-Molecular-Weight Aromatic Polyacetylenes with [Rh(norbornadiene)Cl]2-Triethylamine and Solvent-Induced Crystallization of the Obtained Amorphous Polyacetylenes, *Polym. J.*, 1991, **23**(9), 1135–1138.

49 M. Itakura, K. Sato, M. A. Lusenkova, S. Matsuyama, K. Shimada, T. Saito and S. Kinugasa, Molecular weight dependency of refractive index increment of polystyrene determined by uniform oligomers, *J. Appl. Polym. Sci.*, 2004, **94**(3), 1101–1106.

50 W. R. Krigbaum and P. J. Flory, Molecular weight dependence of the intrinsic viscosity of polymer solutions. II, *J. Polym. Sci.*, 1953, **11**(1), 37–51.

51 Y.-Y. Zhou, Y.-C. Xu, Z.-F. Yao, J.-Y. Li, C.-K. Pan, Y. Lu, C.-Y. Yang, L. Ding, B.-F. Xiao, X.-Y. Wang, Y. Shao, W.-B. Zhang, J.-Y. Wang, H. Wang and J. Pei, Visualizing the multi-level assembly structures of conjugated molecular systems with chain-length dependent behavior, *Nat. Commun.*, 2023, **14**(1), 3340.